

Titre: Corrosion behavior and fibrinogen adsorptive interaction of SS316L surfaces covered with ethylene glycol plasma polymer-coated Ti nanoparticles
Title:

Auteurs: Jason Robert Tavares, A. Shahryari, J. Harvey, Sylvain Coulombe, & Sasha Omanovic
Authors:

Date: 2009

Type: Article de revue / Article

Référence: Tavares, J. R., Shahryari, A., Harvey, J., Coulombe, S., & Omanovic, S. (2009). Corrosion behavior and fibrinogen adsorptive interaction of SS316L surfaces covered with ethylene glycol plasma polymer-coated Ti nanoparticles. Surface and Coatings Technology, 203(16), 2278-2287.
Citation: <https://doi.org/10.1016/j.surfcoat.2009.02.025>

Document en libre accès dans PolyPublie

URL de PolyPublie: <https://publications.polymtl.ca/10439/>
PolyPublie URL:

Version: Version finale avant publication / Accepted version
Révisé par les pairs / Refereed

Conditions d'utilisation: Creative Commons Attribution-Utilisation non commerciale-Pas d'oeuvre dérivée 4.0 International / Creative Commons Attribution-NonCommercial-NoDerivatives 4.0 International (CC BY-NC-ND)
Terms of Use:

Document publié chez l'éditeur officiel

Titre de la revue: Surface and Coatings Technology (vol. 203, no. 16)
Journal Title:

Maison d'édition: Elsevier
Publisher:

URL officiel: <https://doi.org/10.1016/j.surfcoat.2009.02.025>
Official URL:

Mention légale: © 2009. This is the author's version of an article that appeared in Surface and Coatings Technology (vol. 203, no. 16) . The final published version is available at <https://doi.org/10.1016/j.surfcoat.2009.02.025>. This manuscript version is made available under the CC-BY-NC-ND 4.0 license <https://creativecommons.org/licenses/by-nc-nd/4.0/>
Legal notice:

Corrosion behaviour and fibrinogen adsorptive interaction of SS316L surfaces covered with ethylene glycol plasma polymer-coated Ti nanoparticles

J. Tavares, A. Shahryari, J. Harvey, S. Coulombe^(a), S. Omanovic^(b)

Department of Chemical Engineering, McGill University,
3610 University Street, Montréal, Québec, H3A 2B2, Canada

^(a) Tel: +1 514 398 5213, Fax: +1 514 398 6678

E-mail: sylvain.coulombe@mcgill.ca

^(b) Tel: +1 514 398 4273, Fax: +1 514 398 6678

E-mail: sasha.omanovic@mcgill.ca

Abstract:

A novel plasma treatment involving the deposition of ethylene glycol plasma polymer-coated titanium nanoparticles on a 316L stainless steel surface is presented. The surface properties of SS316L modified with these coated nanoparticles were compared to untreated SS316L. The deposition of ethylene glycol plasma polymer-coated nanoparticles confers properties to the surface making it more biocompatible, which is beneficial in applications of SS316L as a blood-contacting implant (e.g. vascular stents, heart valves). These properties include increased hydrophilicity and general corrosion resistance of the surface, and reduced substrate-dependent denaturation of adsorbed protein fibrinogen.

PACS codes: 52.80.mg, 52.80.pi, 81.05.zx, 81.07.-b, 81.65.kn, 87.15.hp

Keywords:

[D] Iron alloy, [D] nanostructure, [C] radio frequency (RF), [D] titanium, [X] biomaterials

1. Introduction

Stainless steel 316L (SS316L) is a ubiquitous material for biomedical applications, finding uses, amongst many others, in vascular stents and bone implants due to its reasonably good resistance to corrosion and its favourable mechanical properties [1, 2]. However, for use in biological environments, corrosion and mechanical properties are only part of the equation: the biological response of the implant is also of a significant concern. This is particularly true in the case of blood-contacting implants, where the adhesion of proteins dictates the cascade of post-implantation processes.

Fibrinogen is a serum protein that adsorbs on the implant surface within minutes following implantation. This protein is of particular interest due to its dominant role in clot (thrombus) formation processes [3, 4]. Thrombosis is a common adverse reaction following implantation, leading to a strong inflammatory response and, potentially, to the rejection of the implant. Thrombosis can lead to the death of the patient if the clot ends up in the heart or brain. This problem is of particular importance in coronary stent implantation, due to the continuous exposure of such implants to blood. It has been suggested that inhibiting the adsorption of fibrinogen on the surface could help in minimizing such adverse reactions [5]. However, recent studies have demonstrated that the structure of the adsorbed fibrinogen, rather than its surface concentration, determines the implant's affinity towards thrombus formation (i.e. its hemocompatibility). It has been proposed that the implant's thrombogenicity, i.e. the tendency of the surface to trigger clot formation, is directly proportional to the extent of the adsorbed fibrinogen's denaturation [6, 7].

Several studies have been dedicated to the surface modification of implant materials to promote favourable protein adsorption, while insuring that the corrosion resistance of the substrate remains unaffected or better, is improved. Electrochemical surface passivation has been shown to be an effective method for modifying stainless steel endovascular stents [8-11], particularly through the alteration of the surface-adsorbed fibrinogen's conformation [6]. Alternatively, some studies report on the deposition of highly-ordered self-assembled monolayers (SAMs) to influence the surface chemistry of the stainless steel [12]. Functionalization of the surface can also be achieved via certain plasma treatments, including reactive ion implantation and plasma polymerization [13-15]. The deposition of nanoparticles and nanostructures formation on SS316L have also been employed to improve the surface corrosion resistance and hemocompatibility [16-18].

The objective of the present study is to take a synergetic approach to improve surface biocompatibility by means of plasma synthesis and deposition of coated nanoparticles onto the SS316L. More precisely, the novel surface modification process developed involves the deposition on the SS316L substrate of a thin layer of titanium nanoparticles that have been coated/functionalized with an ethylene glycol-based plasma polymer. The properties of the coated surface are evaluated through an assessment of its topography, hydrophilicity, chemistry, corrosion behaviour, and extent of interaction with fibrinogen.

2. Experimental Protocol

The experimental setup employed to produce coated/functionalized metal nanoparticles and coat the SS316L samples was first discussed in [19] and further detailed in [20]. The

dual-plasma reactor features a concentric geometry favouring the efficient synthesis, in-flight coating and functionalization, as well as the transport of nanoparticles toward the surface to be coated. A metal cathode made of titanium (Ti) is mounted on the centerline of the assembly and exposed to repetitive arcing events (stainless steel bars surrounding the cathode serve as the grounded anode), which lead to the localized evaporation of the surface and formation of a rapidly-expanding metallic vapour plume. Bare Ti nanoparticles are formed at the periphery of the plume through homogenous nucleation followed by growth.

The cathode and anode assembly is surrounded by a stainless steel mesh (5 mm × 5 mm openings) that acts as the live electrode for a radio-frequency (RF) capacitively-coupled glow discharge. Once formed, the nanoparticles generated by the arcing events make their way into this RF discharge which serves two purposes: 1) the deposition of a functional coating onto the surface of the nanoparticles, and 2) the charging (negatively) of the recently formed nanoparticles, which influences the collection and limits agglomeration of the nanoparticles. The SS316L samples are suspended on a collection ring placed after the RF mesh electrode which is held at a positive potential with respect to the ground in order to enhance nanoparticle collection.

The plasma reactor chamber consists of a 4-way cross which can be evacuated to a base pressure of ca. 4 mtorr. Argon is fed into the reactor at a rate of 2000 SCCM (standard cubic centimeter per minute) and the pressure maintained at 20 torr. Ethylene glycol (EG) is used as the plasma polymerizable gas in experiments where a functional coating is

applied to the nanoparticles. EG is fed into the reactor at a concentration of approximately 7×10^{-4} mol percent. Titanium (ASTM B348 Grade 2), a metal known for its relatively good biocompatibility [21], is used as the cathode material. In a typical experiment, the Ti cathode is exposed to 60 cycles of 45 sec of arcing events (approximately 10 per second, 10 msec duration, and 10 A-peak each) followed by 4 min and 45 sec cool-down periods. Each SS316L sample is thus exposed to the nanoparticles stream for a total of 45 min. Note, finally, that the RF plasma is not in contact with the SS316L samples. A schematic representation of the experimental setup is given in Figure 1(a), while Figure 1(b) shows the dual plasma system in operation. An arcing event can be observed at the center; the bright blue light is characteristic of a Ti discharge [22]. A much dimmer RF glow discharge forms between the mesh electrode and the grounded anode; its bluish hue is characteristic of the emission of organic compounds [23].

The SS316L samples consist of 12.7 mm-diameter discs machined to a thickness of 1 mm. Before plasma treatment, the samples are successively polished using 240, 400, 600 and 4000-grit SiC sandpaper. Following this, the samples are immediately (within 2 minutes) suspended on the collection ring of the dual-plasma reactor and exposed to an inert Ar environment at low pressure (20 torr) to minimize re-oxidation of the surface.

After treatment, electrochemical measurements were carried out on the samples using an Ecochemie Autolab PGSTAT30 Potentiostat/Galvanostat, combined with the FRA2 electrochemical impedance spectroscopy (EIS) module. The GPES/FRA v.4.9.5 software was used to control the instrument and for data collection and treatment. A platinum wire

was used as a counter electrode (CE), and the reference electrode (RE) was a saturated calomel electrode (SCE). The bare SS316L surfaces (control), SS316L surfaces coated with bare Ti nanoparticles (Ti), and SS316L surfaces coated with ethylene glycol plasma-coated Ti nanoparticles (Ti+EG) were used as the working electrode (WE). In order to expose only the plasma treated side of the samples to the electrolyte, the WE was placed in a specially constructed electrochemical cell, exposing 0.5 cm^2 of the treated side to the electrolyte. All the electrochemical experiments were performed in an oxygen-free electrolyte, which was achieved by continuously purging the electrolyte with Ar, starting 30 min prior to the measurement and continuing during the measurement. De-ionized (DI) water was used in all experiments.

The electrochemical measurements were conducted sequentially starting with open circuit potential (OCP), for either a period of one hour or until a potential was stabilized to less than a 2 mV min^{-1} change. This step was followed by electrochemical impedance spectroscopy (EIS) measurements at OCP over a frequency range of 10 mHz to 50 kHz. The AC voltage amplitude was set to 10 mV. Potentiodynamic polarization experiments were carried out at a scan rate of 1 mV s^{-1} , starting from 50 mV negative of the OCP and sweeping towards the anodic direction, until a current density of 1 mA cm^{-2} was reached, following by the polarization bias reversal. All measurements were performed at 22 ± 1 °C in 0.16 M aqueous NaCl (Fisher Scientific Certified A.C.S.), which is the chloride concentration equivalent to that in human body fluids. It should be noted that all electrochemical and protein adhesion assays were not conducted under ideal physiological conditions in order to improve reproducibility. The behavior of the samples

under these *in vitro* conditions is sufficient to infer behavior under an *in vivo* environment [24].

The wetting properties of the treated surfaces were assessed by measuring the contact angle of a droplet of DI water on the surface using a Dataphysics Contact Angle System OCA goniometer. Contact angle measurements were performed at the following time intervals: within 1 hour of sample production, after 24 hours, after 7 days and after 14 days. Electron micrographs of the treated surfaces were taken using a Hitachi S4700 FE-SEM and an FEI Tecnai 12 120 kV TEM. Image analysis of the TEM micrographs was performed using the ImageJ 2.10 open-source software. Assessment of the film thickness was achieved using atomic force microscopy (AFM). More precisely, a NT-MDT scanning probe microscope with a SOLVER platform in semi-contact mode was employed; measurements were carried out in air using conductive gold-coated silicon cantilevers (non-contact NSG-10 series, provided by NT-MDT).

Prior to fibrinogen adsorption measurements, the samples were degreased with ethanol and then rinsed with DI water. Phosphate buffer (PB) solution (pH 7.4) of bovine plasma fibrinogen (Sigma-Aldrich Co., Cat. No. F-8630) at a concentration of 0.1 g L^{-1} was used in adsorption measurements. Adsorption of proteins was performed at $22 \pm 1 \text{ }^{\circ}\text{C}$ by immersing the samples in the PB-protein solution for 0 (blank), 2, 15 and 40 min and finally, for 16 hrs. At the end of each time interval, the samples were taken out and then thoroughly rinsed first with DI water to remove loosely adsorbed protein, followed by

dipping in ethanol for a short time. The samples were then left to dry in air and analyzed in a polarization modulation infrared reflection absorption spectrometer (PM-IRRAS).

PM-IRRAS spectra were recorded using a Bruker Optics PMA50 external module attached to the TENSOR 27 FT-IR spectrometer. A liquid nitrogen cooled MCT detector was used in all experiments. The wavelength setting on the Hinds PEM-90 was fixed at 1600 cm^{-1} (the amide region of the protein). The sample was scanned 278 times with a resolution of 3 cm^{-1} and an aperture setting of 6 mm. The incident beam angle (with respect to the surface normal) used in all experiments was 80° . Manipulation of the resulting absorption spectra was performed using the Bruker OPUS Spectroscopy v.5.0 software.

The same TENSOR 27 FT-IR spectrometer was used to characterize the functional groups present on the surface. Mapping of these groups was accomplished using a Bruker Hyperion 2000 microscope with a 2 mm aperture. 20 scans were taken for each $100\text{ }\mu\text{m}$ unit area at a resolution of 4 cm^{-1} recorded from 600 to 4000 cm^{-1} . An untreated SS316L surface was used as a background sample in all cases.

3. Results & Discussion

3.1 Surface topography

When the plasma-treated SS316L samples are removed from the reactor, a dark, soot-like deposit is visible. The dark color of the deposit is characteristic of nanostructured coatings (structures smaller than visible wavelengths). The nanometric nature of the Ti deposits is apparent in the FE-SEM micrographs shown in Figure 2. For comparison, a

micrograph of the non-modified (naked) SS316L surface is presented as Figure 2(a). Figure 2(b) shows bare Ti nanoparticles deposited onto the SS316L substrate; in this case, no organic precursor was injected into the reactor. These uncoated nanoparticles form flake-like agglomerates on the surface. A large, micron-sized particle is also visible on this surface in the centre of the micrograph in Figure 2(b); such larger particulates are a known by-product of the arc erosion process [20]. With the exception of this larger particulate and its immediate surrounding, the SEM analysis has demonstrated that the Ti nanoparticulate coating is uniformly deposited on the SS316L substrate.

Similar observations can be made with the second micrograph, Figure 2(c), which reveals Ti nanoparticles coated with an ethylene glycol plasma polymer and deposited onto the SS316L substrate. While the coating seems similarly uniform, the structure of the agglomerates formed appears finer. This is likely the result of smaller polymeric beads co-deposited onto the surface along with the coated nanoparticles [20, 25]. The organic coating and the polymeric beads can be seen on the TEM micrograph shown in Figure 3(a). The particles deposited onto the substrate have a count mean diameter of 3.5 nm (the calculation of the mean diameter excludes particles smaller than 1 nm and larger than 100 nm). A lower magnification image is shown in Figure 3(b) and its size distribution is shown in Figure 3(c). Atomic force microscopy revealed that the thickness of the deposited coatings is on the order of 1 μm . This assessment was achieved by comparing the thickness of the topographical image from a treated region to that of a masked section of the sample.

3.2 Wetting and surface chemistry

The contact angle of a droplet of DI water on the investigated surfaces was measured immediately after treatment. The average contact angle on a freshly polished sample of SS316L is $57^{\circ} \pm 2^{\circ}$. When a coating of bare Ti nanoparticles is deposited onto the surface, the contact angle decreases to an average value of $40^{\circ} \pm 4^{\circ}$ (however, a t-test with $\alpha=0.05$ has determined that this decrease is not statistically significant). When plasma polymer-coated Ti nanoparticles are deposited onto the stainless steel substrate, the contact angle decreases significantly to values below the detection limit of the goniometer used (less than 5°). While a decrease in apparent contact angle on the Ti samples could be explained by an increase in the surface area, the decrease observed with the Ti+EG samples is a direct result of the hydrophilic nature of plasma polymer deposited onto the Ti nanoparticles. In fact, it has been previously demonstrated that an ethylene glycol plasma polymer coating on Cu nanoparticles produces a hydrophilic surface [20].

The hydrophilic nature of the ethylene glycol plasma polymer treatment is likely a result of the high oxygen-species content in the resulting coating. The oxygen is present mainly in the form of hydroxyl, carboxylic and ketonic functional groups, as illustrated in Figure 4. The peaks present in the $3300\text{-}3500\text{ cm}^{-1}$ range are strongly indicative of OH, while those in the $1670\text{-}1760\text{ cm}^{-1}$ range are related to carbon-oxygen double bonds. More precisely, the peak at 1710 cm^{-1} corresponds to saturated carboxylic acids (-COOH), while the peak at 1685 cm^{-1} is a result of ketones (C=O). Peaks about $1040\text{-}1100\text{ cm}^{-1}$ are related to carbon-oxygen bonds found in alcohols. For ethylene glycol, it is expected that

only the peak for a primary alcohol would be observable (1050 cm^{-1}), however due to apparent overlapping of a number of signals in this region, it is likely that the alcohol groups are located in a wide variety of locations on the polymer, indicating a random and highly cross-linked plasma polymer structure [26]. This is supported by the convolution of the alkyl bond peaks (C-H) in the $1250\text{-}1480\text{ cm}^{-1}$ and $2830\text{-}3000\text{ cm}^{-1}$ regions. The fact that the peaks about 2860 and 2940 cm^{-1} are not resonance-shifted to lower values is indicative of an amorphous structure [26]. Atmospheric CO_2 is apparent at about 2350 cm^{-1} .

Although similar hydrophilic surfaces obtained through plasma deposition or functionalization are subject to hydrophobic recovery, measurements of the contact angle on the Ti+EG surfaces show that these retain their hydrophilic behaviour over time. In fact, the contact angle measured after one week remains below the detection limit of the apparatus. After two weeks, some hydrophobic recovery is observed: the contact angle increases to an average value of $8^\circ \pm 5^\circ$ (which is still well within the super-hydrophilic range). Because the surface wettability directly influences protein adsorption, and thus the surface's thrombogenicity and extent of interaction with cells, it is expected that the super-hydrophilic nature of the Ti+EG deposit will promote more favourable fibrinogen interaction with the surface, when compared to naked SS316L [27, 28], which is indeed evidenced later in the paper.

3.3 Corrosion properties

SS316-based biomaterials should exhibit high resistance to localized and general corrosion to protect against mechanical failure and the release of toxic ions in local tissue, respectively (Cr ions are carcinogenic and mutagenic, while Ni ions are carcinogenic and allergenic) [29]. Thus, to study the corrosion behavior of the control, Ti and Ti+EG-nanoparticles covered samples, the coupons were immersed in a 0.16 M NaCl solution and subjected to three tests: open-circuit potential (OCP), electrochemical impedance spectroscopy (EIS) and potentiodynamic polarization (PP).

Initial information on the general corrosion stability of the investigated surfaces was obtained by monitoring the OCP (Figure 5). In general, more negative OCP values indicate an increased general corrosion activity (dissolution) of the surface [30]. Figure 5 shows that, in all experiments, a quasi-equilibrium OCP value is reached after one hour. However, Ti and Ti+EG nanoparticle-covered surfaces reach a more positive quasi-equilibrium OCP value (-41 mV and -219 mV, respectively) than the control surface (-277 mV). This indicates an increased general corrosion resistance of the covered surfaces [30], and is in agreement with other works conducted on Ti-based coatings on SS316L [31, 32]. Namely, OCP represents a mixed (corrosion) potential of the cathodic (hydrogen evolution in this case) and anodic (metal dissolution) reaction occurring when no total current flows through the cell. Since Ti forms a barrier-type corrosion-resistant TiO_2 film on its surface and the ethylene glycol plasma polymer coating is an insulator, it is expected that the measured OCP of these two surfaces would be more noble than that of the control (SS316L) surface [33, 34].

To further investigate the samples' general corrosion properties, EIS experiments were performed. The Bode representations of the EIS spectra, recorded at OCP, are presented in Figure 6. A two-time constants equivalent electrochemical circuit (EEC), presented in Figure 6(c), was used to fit the experimental data. The elements of the EEC used have the following meanings: R_{EL} is the resistance of the electrolyte, R_1 and R_2 stand for the electron-transfer and charge (ion) transport resistances and; CPE_1 and CPE_2 are constant phase elements with exponent n representing a degree of deviation from pure capacitive, resistive or inductive behavior, due to macroscopic inhomogeneities in the passive film and at the oxide/electrolyte interface [11, 35]. Depending on the exponent n , the CPE can represent different components: if $n = 1$, an ideal capacitor; if $n = 0.5$, a Warburg diffusion element; if $n = 0$, an ohmic resistor and; if $n = -1$, an inductor. The values calculated for the various elements of the EEC used to fit the experimental data are presented in Table 1.

Figure 6 shows that there is a good agreement between the experimental data (symbols) and the model (solid line), validating the use of the proposed EEC in modeling. The two different time constants in the proposed EEC indicate that there are two sets of surface processes characterized by different time constants. The components CPE_2 and R_2 are associated with processes occurring at low frequencies (such as transport of charged species, ions, through a passive SS316L and Ti film and a deposited polymer coating), while CPE_1 and R_1 represent higher-frequency processes related to charge separation in the passive film and electron-transfer, respectively. Table 1 shows that CPE_1 represents capacitance (average $n = 0.93 \pm 0.01$), while the value of the CPE_2 exponent (average

$n = 0.69 \pm 0.08$) is between the value characterizing pure capacitance and pure Warburg diffusion element. Hence, it could be assumed that CPE_2 is related to the charge gradient across the passive film (capacitive contribution) originating from the diffusion of dissolved metal ions from the metal/passive film to the passive film/electrolyte interface (Warburg contribution).

The polarization resistance, R_p , is the sum of R_1 and R_2 and represents a measure of the resistance to general corrosion. Table 1 shows that the trend of polarization resistance (and thus the general corrosion resistance) is similar to the OCP trend in Figure 5. Namely, in both figures, the control surface (SS316L) offers the lowest general corrosion resistance, followed by the Ti+EG surface, and then the Ti surface. In fact, if the polarization resistance values in Table 1 were normalized to the true surface area accessible to the corrosive electrolyte, the resulting true corrosion resistance of the Ti and Ti+EG surfaces would be much greater, since the two nanoparticles-covered surfaces have a significantly higher surface area than the control SS316L surface (Figure 2). In summary, the OCP and EIS results demonstrate that the modification of the SS316L surface with Ti and Ti+EG nanoparticles results in an improvement of general corrosion resistance of the surface, which is beneficial for biomedical applications of the material.

As mentioned previously, resistance of SS316-based implants to localized corrosion is of significant importance since this can influence the mechanical stability of the implant. In the case of SS316-based vascular stents, the resistance of the stent to localized corrosion could be a question of life or death, since it has been shown that even more biocompatible NiTi stents undergo significant pitting corrosion and subsequent structural

failure when implanted in animal models [36]. In the case of Ti and Ti+EG coatings on the SS316L surface studied here, one can suspect that the nanoparticles covered surface could be less resistant to localized corrosion than the control SS316L surface. This is due to the presence of nano-pores on the former two surfaces (Figure 2), which are good sites for initiation of localized corrosion of the nanoparticles-free (uncovered) parts of the SS316L substrate, due to a high possibility for a local pH drop and increase in concentration of highly-corrosive chloride species inside these nano-pores. Thus, to compare the localized corrosion stability of the two nanoparticles modified surfaces to the control surface, potentiodynamic polarization (PP) tests were performed [8-11, 37].

Figure 7(a) shows typical cyclic polarization curves of the Ti, Ti+EG and control surfaces. Figure 7(b) shows the potential difference (ΔV) between the SS316L passive oxide film breakdown potential (E_B) and OCP. The breakdown potential (E_B) is defined as the potential at which the current suddenly increases in the cyclic polarization curve. It should be remembered that breakdown of Ti-oxide passive films occurs at much higher anodic potentials [38, 39], so the breakdown potentials in this work are related only to the breakdown of passive oxide films grown on the SS316L substrate surface. In Figure 7(b), the overlap of the 95% confidence intervals indicates that the film breakdown potential of the Ti and Ti+EG surfaces is not significantly different from that of the control surface. It is pertinent to note that, after testing, corroded rings were observed where the polytetrafluoroethylene (PTFE) and rubber gasket were in contact with the surface and the solution. The electron micrograph shown in Figure 8 illustrates the crevice formed. The crevices were likely a result of stagnant zones induced by the cell geometry. In fact,

it has been shown that the accumulation of chloride ions can greatly increase their rate of surface diffusion and promote crevice formation [40]. Aside from the crevice corrosion rings, visual inspection and further SEM imaging showed a smooth surface, free of localized pitting. However, it should be noted that the passive current on the Ti and Ti+EG surfaces is significantly lower than on the control surface (up to an order of magnitude, depending on the potential region), indicating a higher general corrosion stability of the nanoparticles-covered surfaces even at anodic potentials significantly more positive than OCP.

The results in Figure 7 demonstrate that the modification of the SS316L surface with Ti and Ti+EG nanoparticles does not significantly influence the material's *localized* corrosion stability. Other studies involving the deposition of TiO₂ nanoparticles on SS316L have led to enhanced resistance to corrosion [16]. The observed corrosion resistance improvement was attributed to the hydrophobic behavior exhibited by these surfaces. However, hydrophobic surfaces are less suited for biomedical applications; as previously mentioned, it has been shown that hydrophilicity is a key requirement for desirable response of the surface to proteins and cells [27, 28]. Although the Ti+EG modified SS316L surface is actually super-hydrophilic, the corrosion measurements presented in Figures 5 to 7 demonstrate that this increase in hydrophilicity does not negatively influence the corrosion stability of the material. On the contrary, the modified surfaces are more resistant to general corrosion. Thus, the increased hydrophilicity of the two nanoparticle-modified surfaces, together with the increased surface roughness

(Figure 2) and general corrosion resistance (Figures 5 and 6) indicate an increased biocompatibility of the materials [41].

3.4 Protein (fibrinogen) adsorption

As mentioned earlier, one of the main criteria determining the level of biocompatibility of a blood-contacting implant is the resistance of its surface toward thrombus (clot) formation. Serum protein fibrinogen (Fg) plays a critical role in the coagulation process by mediating the adhesion of platelets onto the surface through a complex chain of biochemical processes [3, 7, 42, 43]. Therefore, the interaction of Fg with an implant surface is commonly evaluated when investigating the biocompatibility of the implant.

Investigation of the surface-adsorbed proteins using PM-IRRAS is based on the evaluation of Amide I and II spectra. These two bands, characteristic of all proteins, originate from the different vibration modes of the polypeptides that compose the proteins [44-46]. Figure 9 shows typical Fg PM-IRRAS spectra recorded on SS316L samples after various immersion times in a Fg solution. The integrated intensity of the amide bands increases with immersion time, indicating that the surface concentration of Fg adsorbed on the SS316L surface also increases. Further analysis of the adsorbed Fg was focused on the Amide I band of the PM-IRRAS spectra, due to its strong and well-defined signal. Moreover, it offers the added possibility of later extracting information on the secondary structures of the surface-adsorbed Fg molecules [44, 45].

The amount of Fg adsorbed on the surface was determined by integrating the area under the Amide I band in the PM-IRRAS spectra (integrated intensity). In order to better evaluate the amount of adsorbed Fg, the changes in the total quantity of Fg adsorbed over time on Ti, Ti+EG and control surfaces are compared in Figure 10. It is important to note that the integrated intensity values presented in the figure represent values with respect to projected (geometrical) surface area of the samples, not the true surface area. The figure shows that the surface-adsorbed amount of Fg increases with time. The presented data also indicate that the difference between the amount of Fg adsorbed on the Ti and Ti+EG surfaces is insignificant at the investigated time intervals. Although the average amount of Fg on these two surfaces is higher than the amount on the control surface, the statistical analysis of the data shows that the only significant difference (between the Ti or Ti+EG and control surfaces) was found at 15 min of immersion time. On the other hand, a similar comparison following 40 min and 16 hr of immersion shows that the increase in the amount of Fg adsorbed on the surface after 16 hours is not significant ($p>0.05$). This confirms that the variation of fibrinogen content with time on all surfaces levels off into a plateau following 40 min of immersion.

However, it is pertinent to note that the actual surface area of the Ti and Ti-EG samples is significantly higher (Figure 2). Thus, if one normalized the amount of protein adsorbed on all three surfaces (Figure 10) with respect to the *true* surface area, the normalized amount of adsorbed Fg would be significantly lower on the Ti and Ti+EG surfaces. This is of significant importance considering the size of the fibrinogen molecule [28, 44, 45] and the geometry of nano-pores produced in the Ti and Ti+EG surfaces. In other words,

although the total amount of Fg per *geometric* (projected) area is higher on the coated surfaces than on the control surface (Figure 10), a large proportion of the adsorbed protein is not accessible to platelets due to the significantly larger size of platelets (2-3 μm) compared to the inter-particle spacing ('pore' size of 50 to 100 nm, see Figure 3). Thus, only Fg adsorbed on the 'outer surface' of the nanoparticles should play a role in platelet/surface interactions. Therefore, taking the results in Figures 2, 3 and 10, one can conclude that the Ti and Ti+EG surfaces should offer a decreased level of thrombogenicity, when compared to the naked (control) SS316L surface.

As discussed earlier, the surface structure of adsorbed Fg plays a determining role in the reactivity of the surface toward platelets activation and thus, it controls the level of thrombogenicity of the surface [6, 7]. The surface conformation depends, in turn, on the secondary structure of adsorbed Fg. Thus, by evaluating the secondary structure of Fg adsorbed on the three investigated surfaces, and comparing it to the secondary structure of Fg in its native (non-thrombogenic) state, one can evaluate the relative degree of thrombogenicity of the surfaces. For this purpose, further analysis of the Amide I peak was performed, since this peak is actually a composite of various overlapping subcomponent bands that each represents different secondary structures of the protein (helices, β -structures, turns and random structures) [44, 45]. The wavenumber regions corresponding to the IR response of each secondary structure is presented in Table 2.

Figure 11 shows an example of the Amide I band fitted with its resulting component peaks. It can be seen that the sum of the fitted underlying component bands (dashed lines)

yields a simulated Amide I band (solid line) that is in very good agreement with the experimental band contour (symbols). A good agreement was also observed for the spectra recorded at other adsorption times. This allows for comparison of the variations in the secondary structure distribution of Fg adsorbed on the investigated surfaces.

The secondary structure of fibrinogen adsorbed on the treated and untreated surfaces following a 40 min immersion was determined. This time point was selected since it corresponds to a time sufficient for the adsorbed protein layer to reach a semi-equilibrium state, so that the secondary structure of adsorbed Fg no longer changes. For comparison, the distribution of the secondary structure of Fg in its native state has also been obtained from the literature [47-49]. It has been shown that the extent of Fg denaturation resulting from adsorption onto an implant surface determines the susceptibility of the surface to platelet adhesion and activation and thus, its thrombogenicity [6, 7]. More precisely, the closer the secondary structure of the adsorbed Fg to that of the native structure, the lower the resulting surface thrombogenicity. The extent of denaturation can be assessed by comparing the ratio of α -helix-to- β -turn structures in the native Fg to that of the Fg adsorbed onto the surface [6, 7]. Figure 12 graphically illustrates the α -helix-to- β -turn and the β -sheet-to- β -turn ratios for the control, Ti and Ti+EG surfaces, and compares them to the ratio of the native structure. The values obtained for the control surface (SS316L) demonstrate that Fg undergoes major secondary structure changes following its adsorption on the substrate. However, the significantly higher α -helix-to- β -turn and also a higher β -sheet-to- β -turn ratios on the Ti+EG surface evidence a secondary structure that is closer to the native state. This is expected to result in a lower attachment of platelets on

the Ti+EG surface and thus, to a lower thrombogenicity. It should be noted that the basis for this conclusion is the authors' recent observations with regards to secondary structure changes of Fg adsorbed on a SS316L surface passivated using various methods, which were verified with subsequent platelets attachment experiments [6]. These secondary structure changes were directly linked to the platelet/surface interactions and surface thrombogenicity.

4. Conclusions

The surface properties of SS316L coated with bare titanium nanoparticles and ethylene glycol plasma polymer-coated titanium nanoparticles were compared to untreated SS316L. It was found that the deposition of ethylene glycol plasma polymer-coated titanium nanoparticles onto SS316L confers properties to the surface making it more suitable for applications as blood-contacting implants. These properties include increased hydrophilicity and general corrosion resistance of the surface without any major adverse impact on the localized corrosion resistance. Moreover, it has been shown that the secondary structure of the fibrinogen protein adsorbed onto this surface is closer to the native structure of fibrinogen. The novel plasma treatment used to produce such coatings is expected to enhance the overall biocompatibility of the investigated SS316L surface.

Acknowledgements:

The authors acknowledge the financial support from the Natural Sciences and Engineering Research Council of Canada (NSERC), the Canadian Institutes of Health

Research (CIHR), the Fonds québécois de la recherche sur la nature et les technologies (FQRNT) and McGill University.

References:

1. J.C. Palmaz: American Journal of Roentgenology 160 (1993) 613
2. J.J. Jacobs, J.L. Gilbert, R.M. Urban: Journal of Bone and Joint Surgery 80-A-2 (1998) 268
3. K.C. Dee, D.A. Puleo, R. Bizios: *An Introduction to tissue-biomaterial interactions* (2003) A John Wiley & Sons Inc., Hoboken, New Jersey
4. K.A. Moskowitz, B. Kudryk, B.S. Collier: Journal of Thrombosis and Haemostasis 79 (1998) 824
5. B.S. Collier, J.L. Kutok, L.E. Scudder, D.K. Galanakis, S.M. West, G.S. Rudomen, K.T. Springer: Journal of Clinical Investigation 92 (1993) 2796
6. A. Shahryari: Ph.D. thesis (2008) McGill University
7. J.N. Lindon, G. McManama, L. Kushner, E.W. Merrill, E.W. Salzman: Blood 68 (1998) 355
8. A. Shahryari, W. Kamal, S. Omanovic: Materials Letters 62 (2008) 3906
9. A. Shahryari, S. Omanovic: Electrochemistry Communications 9 (2007) 76
10. A. Shahryari, S. Omanovic, J.A. Szpunar: Materials Science and Engineering C 28 (2008) 94
11. A. Shahryari, S. Omanovic, J.A. Szpunar: Journal of Biomedical Materials Research A (2008) in press
12. A. Mahapatro, D.M. Johnson, D.N. Patel, M.D. Feldman, A.A. Ayon, C.M. Agrawal: Nanomedicine: Nanotechnology, Biology and Medicine 2 (2006) 182
13. F. Zhang, E.T. Kang, K.G. Neoh, P. Wang, K.L. Tan: Biomaterials 22 (2001) 1541
14. G.P. Lopez, B.D. Ratner, R.J. Rapoza, T.A. Horbett: Macromolecules 26-13 (1993) 3247
15. N. Gomathi, A. Sureshkumar, S. Neogi: Current Science 94-11 (2008) 1478
16. G.X. Shen, Y.C. Chen, L. Lin, C.J. Lin, D. Scantlebury: Electrochimica Acta 50 (2005) 5083
17. H. Yun, J. Li, H.B. Chen, C.J. Lin: Electrochimica Acta 52 (2007) 6679
18. M. Okada, M. Masuda, R. Tanaka, K. Miyatake, D. Kuroda, T. Furuzono: Journal of Biomedical Research A 83-3 (2007) 589
19. E.J. Swanson, J. Tavares, S. Coulombe: IEEE Transactions on Plasma Science 36-4 (2008) 886
20. J. Tavares, E.J. Swanson, S. Coulombe: Plasma Processes and Polymers 5 (2008) 759
21. D.M. Brunette, P. Tengvall, M. Textor, P. Thomsen: *Titanium in Medicine* (2001) Springer 1st edition
22. CRC Handbook of Chemistry and Physics
23. Y. Wang, J. Zhang: Journal of Macromolecular Science B 45 (2006) 899
24. D.C. Hansena: The Electrochemical Society's Interface 17-2 (2008) 31
25. C. Qin, S. Coulombe: Plasma Sources Science and Technology 16 (2007) 240
26. J. Coates: *Encyclopedia of Analytical Chemistry, Interpretation of Infrared Spectra* (2000) John Wiley & Sons Inc., Chichester
27. L. Chenglong, Y. Dazhi, L. Guoqiang, Q. Min: Materials Letters 59 (2005) 3813

28. S. Tunc, M.F. Maitz, G. Steiner, L. Vázquez, M.T. Pham, R. Salzer: Colloids and Surfaces B: Biointerfaces 42 (2005) 219
29. Y. Okazaki, E. Gotoh: Biomaterials 26 (2005) 11
30. S. Omanovic SG. Roscoe: Journal of Colloid and Interface Science 227, 2 (2000), 452
31. T. Sundararajan, U.K. Mudali, K.G.M. Nair, S. Rajeswari and M. Subbaiyan: Materials and Corrosion 50 (1999) 344
32. M.H. Fathi, M. Salehi, A. Saatchi, V. Mortazavi, S.B. Moosavi: Dental Materials 19 (2003) 188
33. I. Gurappa: Materials Characterization 49 (2002) 73
34. L. Reclaru, J.M. Maeyer: Biomaterials 19-1-3 (1998) 85
35. X. Cheng, S.G. Roscoe: Biomaterials 26 (2005) 7350
36. C. Heintz, G. Riepe, L. Birken, E. Kaiser, N. Chakfe, M. Morlock, G. Delling, H. Imig: Journal of Endovascular Therapy 8 (2001) 248
37. Z. Bou-Saleh, A. Shahryari, S. Omanovic: Thin Solid Films 515 (2007) 4727
38. Y. Okazaki, Y. Ito, K. Kyo, T. Tateishi: Materials Science and Engineering A 213-1-2 (1996) 138
39. A.K. Vijh: Corrosion Science 13-10 (1973) 805
40. S.A. Bradford: *Corrosion Control* (2001) 2nd ed., CASTI Publishing, Edmonton, 1-51
41. D. Buser, R.K. Schenk, S. Steinemann, J.P. Fiorellini, C.H. Fox, H. Stich: Journal of Biomedical Materials Research 26-6 (1992) 831
42. A.B. Anderson, T.H. Tran, M.J. Hamilton, S.J. Chudzik, B.P. Hastings, M.J. Melchior, R.W. Hergenrother, American Journal of Neuroradiology 17 (1996) 859
43. K. Muramatsu, M. Uchida, H.-M. Kim, A. Fujisawa, T. Kokubo, Journal of Biomedical Materials Research 65A (2003) 409
44. M.J. Desroches, N. Chaudhary, S. Omanovic: Biomacromolecules 8 (2007) 2836
45. M.J. Desroches, S. Omanovic: Physical Chemistry Chemical Physics 10 (2008) 2502
46. B. Stuart: *Infrared Spectroscopy: Fundamentals and Applications* (2004) John Wiley & Sons Inc., Chichester
47. S. Tunc, M.F. Maitz, G. Steiner, L. Vazquez, M.T. Pham, R. Salzer: Colloids and Surfaces B: Biointerfaces 42-3-4 (2005) 219
48. I. Azpiazu, D. Chapman: Biochimica et Biophysica Acta- Protein Structure and Molecular Enzymology 1119-3 (1992) 268
49. C. Yongli, Z. Xiufang, G. Yandao, Z. Nanming, Z. Tingying, S. Xinqi: Journal of Colloid Interface Science 214-1 (1999) 38

Figure captions:

Figure 1: (a) Schematic representation of the experimental setup illustrating the trajectories of the nanoparticles expelled from the metallic vapor plume. (b) Picture of the dual plasma region, showing both the Ti arc discharge and the RF glow discharge.

Figure 2: FE-SEM micrographs of (a) an untreated (naked) SS316L surface, (b) bare Ti nanoparticles and (c) Ti nanoparticles coated with an ethylene glycol plasma polymer deposited onto a SS316L substrate.

Figure 3: (a) TEM micrograph of ethylene glycol plasma polymer coated Ti nanoparticles showing the organic layer coating the particles and polymeric beads; (b) a lower magnification TEM micrograph of the same sample and; (c) the particle size distribution in (b).

Figure 4: FT-IR microscopy reflection spectrum identifying the various functional groups that are characteristic of a Ti+EG sample.

Figure 5: Open circuit potential (OCP) of coated and uncoated SS316L substrates as a function of time. The experiments were performed in 0.16 M NaCl solution. Temperature = 22 °C.

Figure 6: Bode plots showing the dependence on frequency of (a) the impedance and (b) the negative phase angle at OCP for control, Ti and Ti+EG samples; (c) the EEC used to model the data (in both Bode plots, the experimental data are presented as symbols and the modeling results are presented as a solid line). The experiments were performed in 0.16 M NaCl solution. Temperature = 22 °C.

Figure 7: (a) Linear polarization curves for control, Ti and Ti+EG samples; (b) potential difference between passive film breakdown (E_B) and OCP (error bars represent 95% confidence intervals). The experiments were performed in 0.16 M NaCl solution. Temperature = 22 °C.

Figure 8: FE-SEM micrograph of a crevice generated during pitting corrosion measurements.

Figure 9: Typical PM-IRRAS spectra of the SS316L following immersion in phosphate buffer solution (pH 7.4) containing 0.1 g L⁻¹ of Fg after (a) 0, (b) 2, (c) 15, (d) 40 min and (e) prolonged immersion of 16 hours. Temperature = 22 °C.

Figure 10: Variation of the Amide I integrated intensity ($A_{\text{amide I}}$) of Fg with immersion time. The data represent the area of the Amide I band of the PM-IRRAS spectra of the control, Ti and Ti+EG surfaces following immersion in phosphate buffer solution (pH 7.4) containing 0.1 g L⁻¹ of Fg. The integrated intensity values refer to the projected surface area of the samples. Temperature = 22 °C.

Figure 11: Amide I band and the underlying resolved components. The experimental PM-IRRAS spectrum (circle symbols) is that of the SS316L surface after a 40 min immersion in a phosphate buffer solution (pH 7.4) containing 0.1 g L⁻¹ of Fg. The sum of the fitted component bands (dashed lines) is presented by the overall simulated Amide I band (solid line). The resolved components are: (1) β -sheet, (2) α -helix, (3) β -turns, (4) contribution of CO_{COOH} stretching modes of –COOH groups in acidic amino acids (Asp and Glu).

Figure 12: Ratio of the Fg secondary structure when adsorbed on the control, Ti and Ti+EG surfaces, with respect to native Fg.

Tables:

Table 1: Impedance parameters for Ti, Ti+EG and control (SS316L) surfaces

	R_{EL} [$\Omega \text{ cm}^2$]	R_1 [$k\Omega \text{ cm}^2$]	R_2 [$k\Omega \text{ cm}^2$]	R_p [$k\Omega \text{ cm}^2$]
Control	68 ± 0	1 ± 0	323 ± 4	324 ± 4
Ti	65 ± 1	250 ± 30	980 ± 30	1230 ± 60
Ti+EG	70 ± 1	80 ± 20	440 ± 3	520 ± 20

	CPE_1		CPE_2	
	[($M\Omega$) $^{-1}s^n\text{cm}^{-2}$]	n	[($M\Omega$) $^{-1}s^n\text{cm}^{-2}$]	n
Control	33 ± 2	0.94 ± 0.01	21 ± 3	0.72 ± 0.01
Ti	23 ± 0	0.91 ± 0.00	15 ± 3	0.62 ± 0.07
Ti+EG	51 ± 0	0.93 ± 0.01	23 ± 1	0.74 ± 0.04

Table 2: Wavenumber range and corresponding secondary structure positions for fitted Amide I component bands applied for the secondary structure studies of adsorbed Fg [44, 45]

Wavenumber [cm^{-1}]	Secondary Structure
1630-1639	β -sheet
1652-1659	α -helix
1675-1685	β -turn
>1695	CO_{COOH} stretching for Asp and Glu COOH side chains

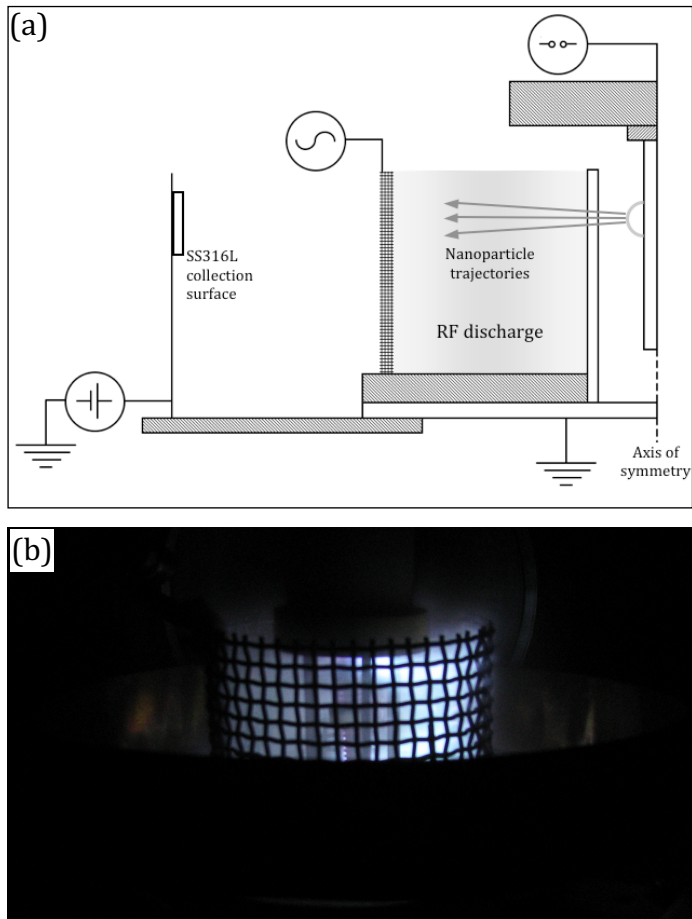


Figure 1: (a) Schematic representation of the experimental setup illustrating the trajectories of the nanoparticles expelled from the metallic vapor plume. (b) Picture of the dual plasma region, showing both the Ti arc discharge and the RF glow discharge.

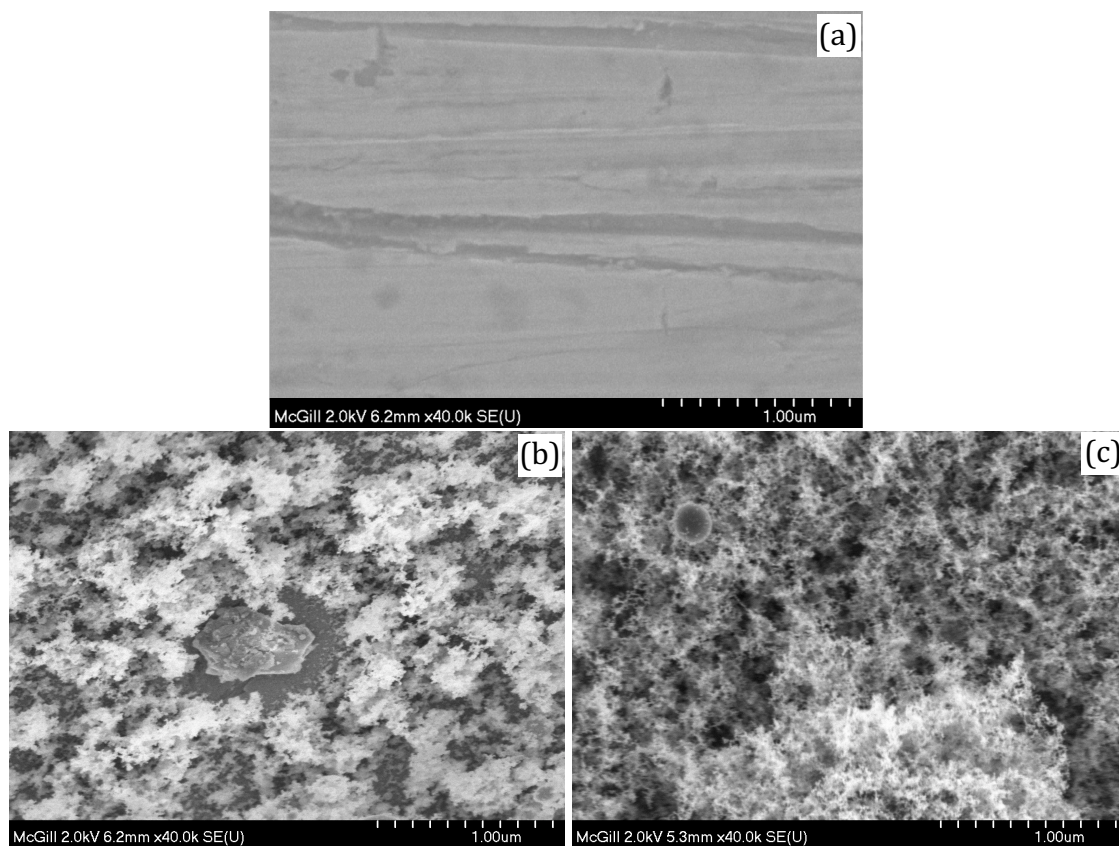


Figure 2: FE-SEM micrographs of (a) an untreated (naked) SS316L surface, (b) bare Ti nanoparticles and (c) Ti nanoparticles coated with an ethylene glycol plasma polymer deposited onto a SS316L substrate.

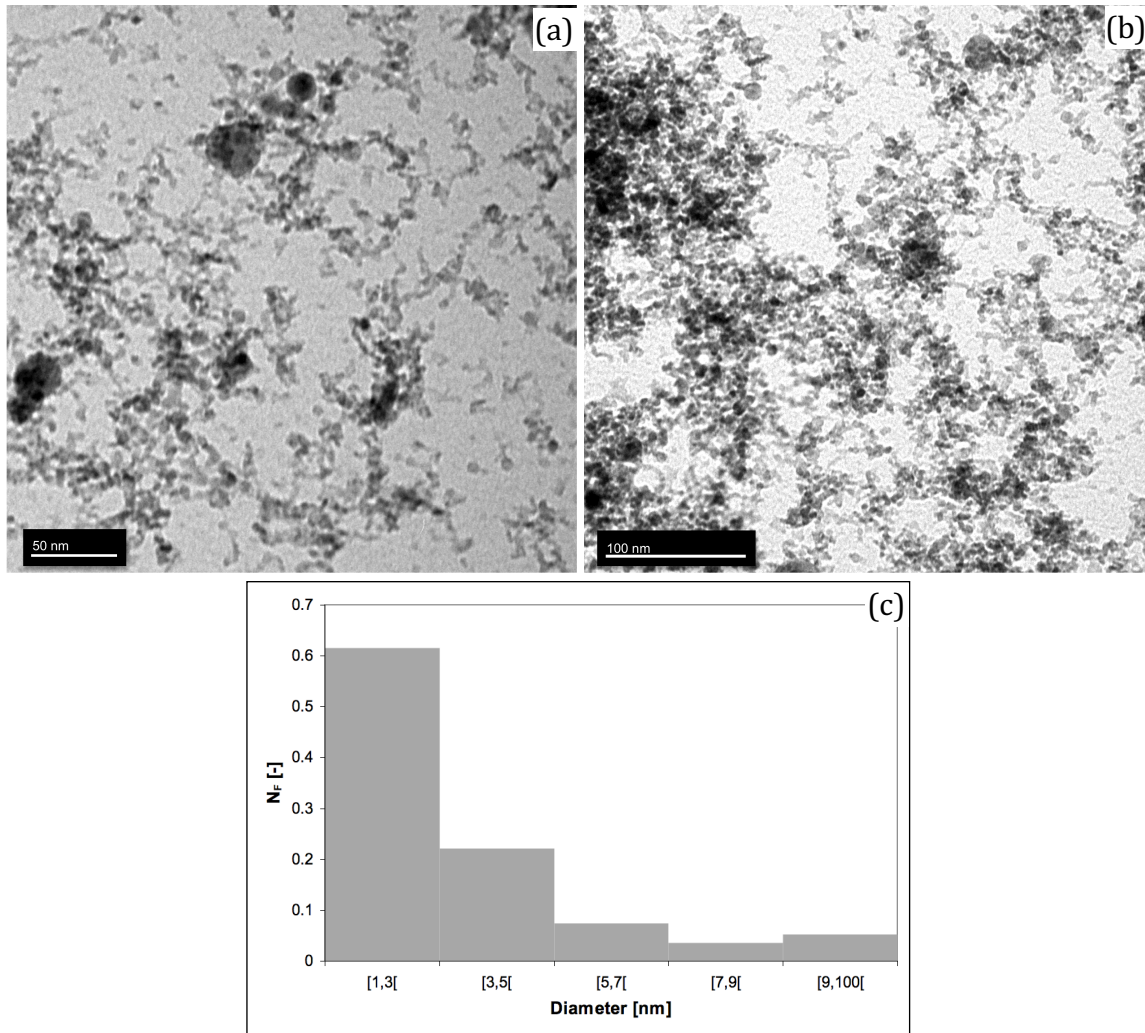


Figure 3: (a) TEM micrograph of ethylene glycol plasma polymer coated Ti nanoparticles showing the organic layer coating the particles and polymeric beads; (b) a lower magnification TEM micrograph of the same sample and; (c) the particle size distribution in (b).

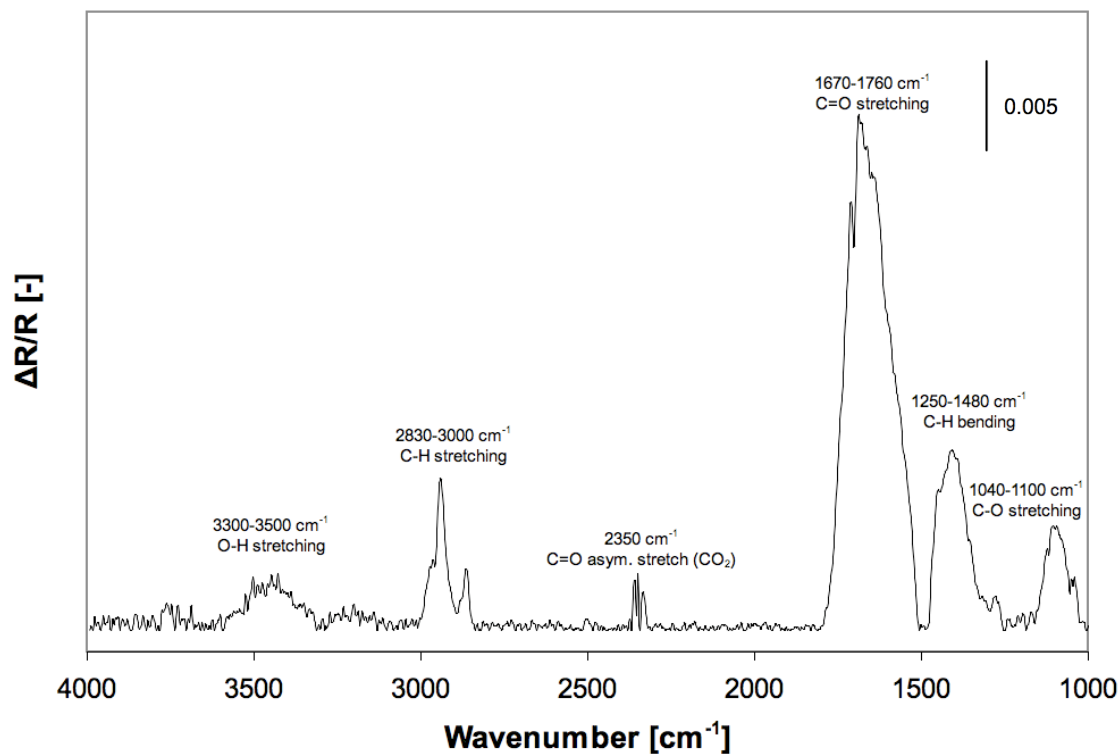


Figure 4: FT-IR microscopy reflection spectrum identifying the various functional groups that are characteristic of a Ti+EG sample.

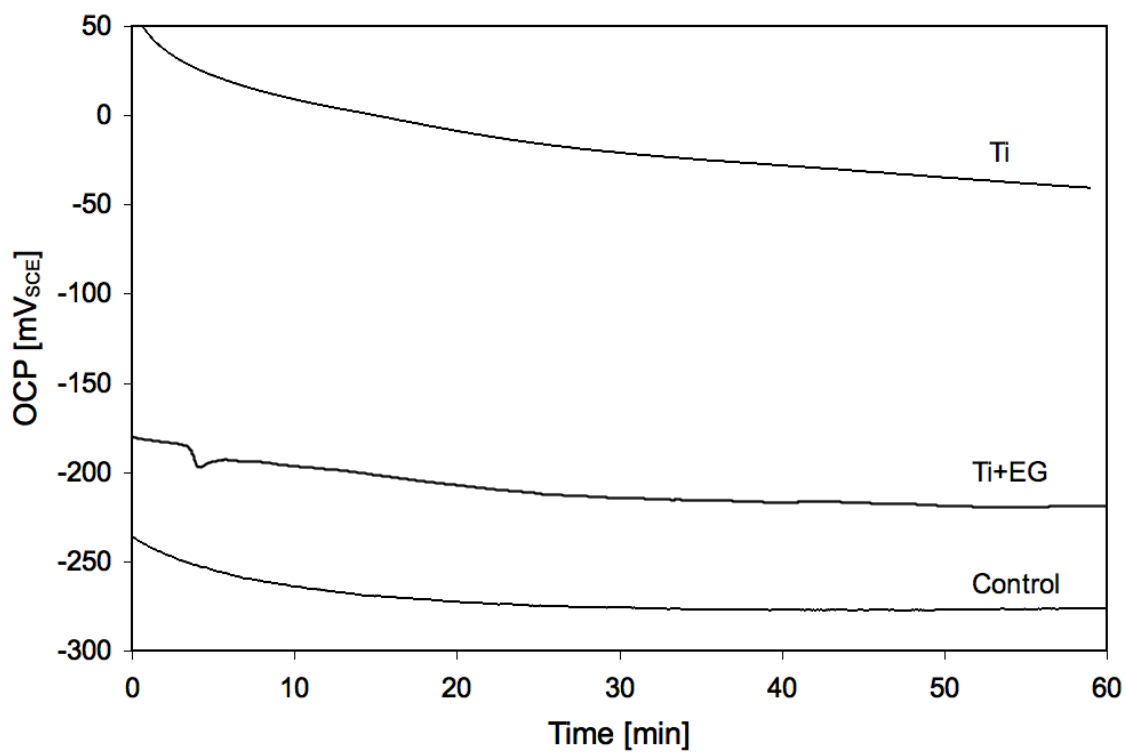


Figure 5: Open circuit potential (OCP) of coated and uncoated SS316L substrates as a function of time. The experiments were performed in 0.16 M NaCl solution. Temperature = 22 °C.

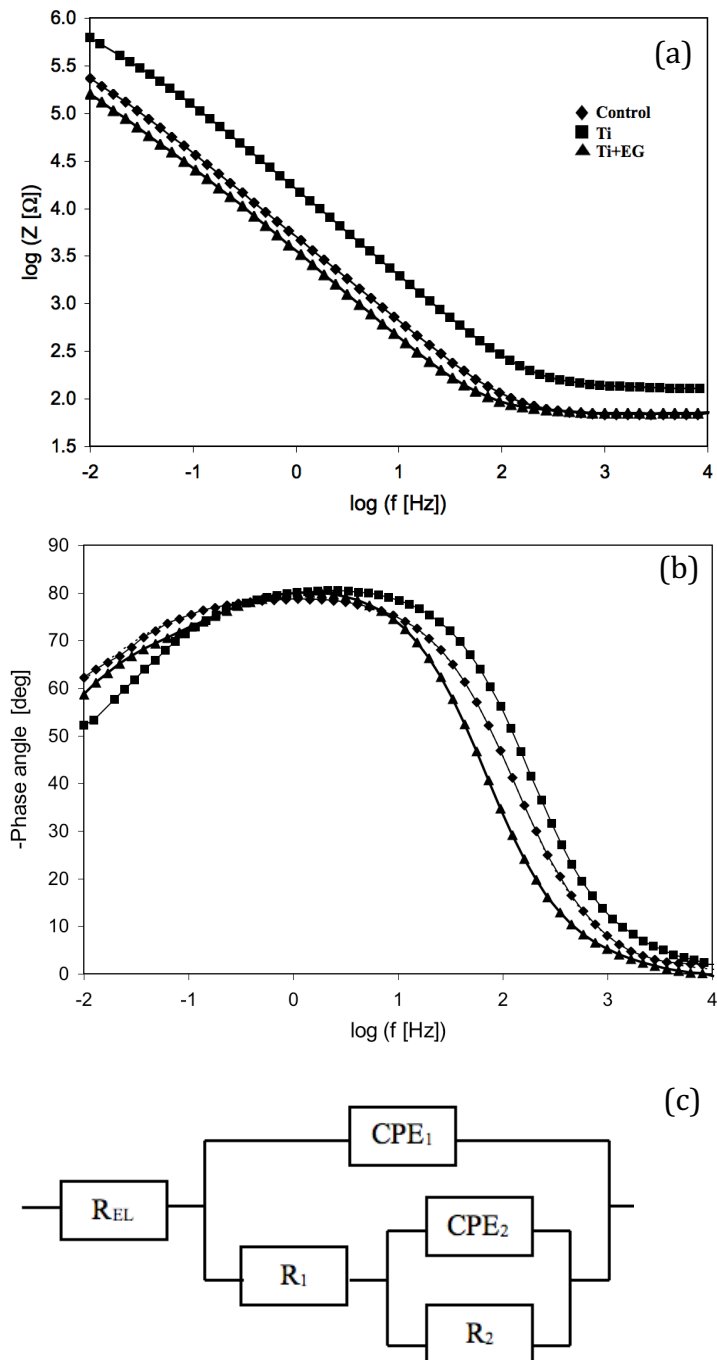


Figure 6: Bode plots showing the dependence on frequency of (a) the impedance and (b) the negative phase angle at OCP for control, Ti and Ti+EG samples; (c) the EEC used to model the data (in both Bode plots, the experimental data are presented as symbols and the modeling results are presented as a solid line). The experiments were performed in 0.16 M NaCl solution. Temperature = 22 °C.

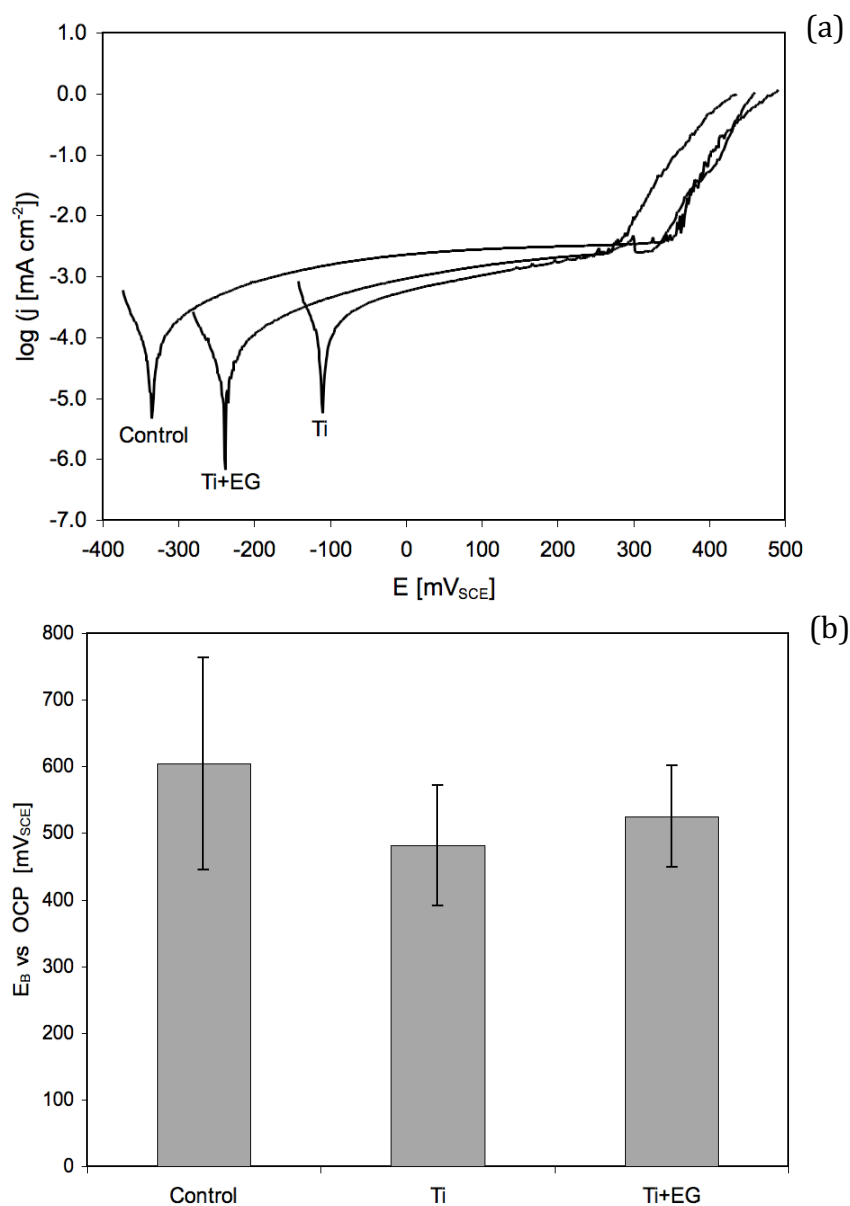


Figure 7: (a) Linear polarization curves for control, Ti and Ti+EG samples; (b) potential difference between passive film breakdown (E_B) and OCP (error bars represent 95% confidence intervals). The experiments were performed in 0.16 M NaCl solution. Temperature = 22 °C.

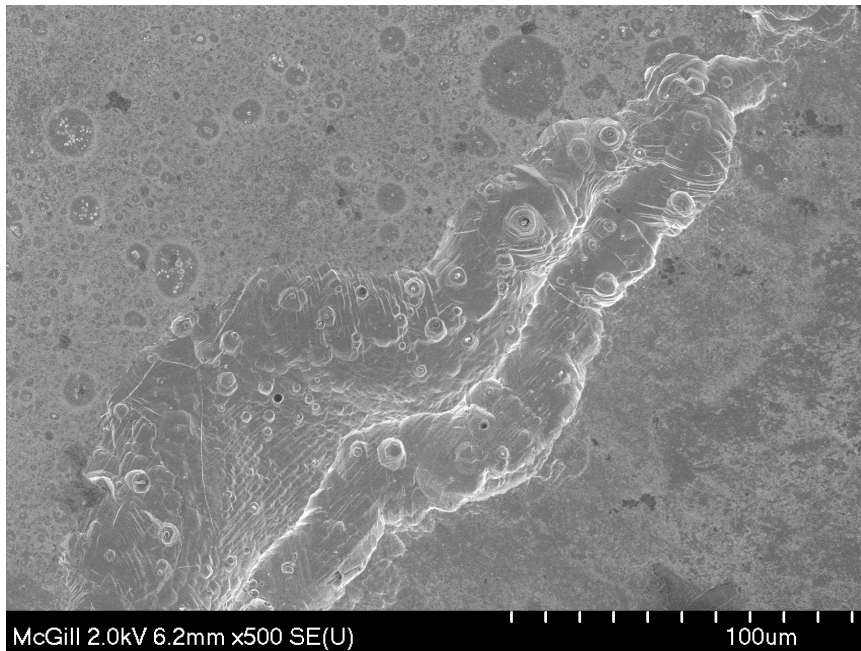


Figure 8: FE-SEM micrograph of a crevice generated during pitting corrosion measurements.

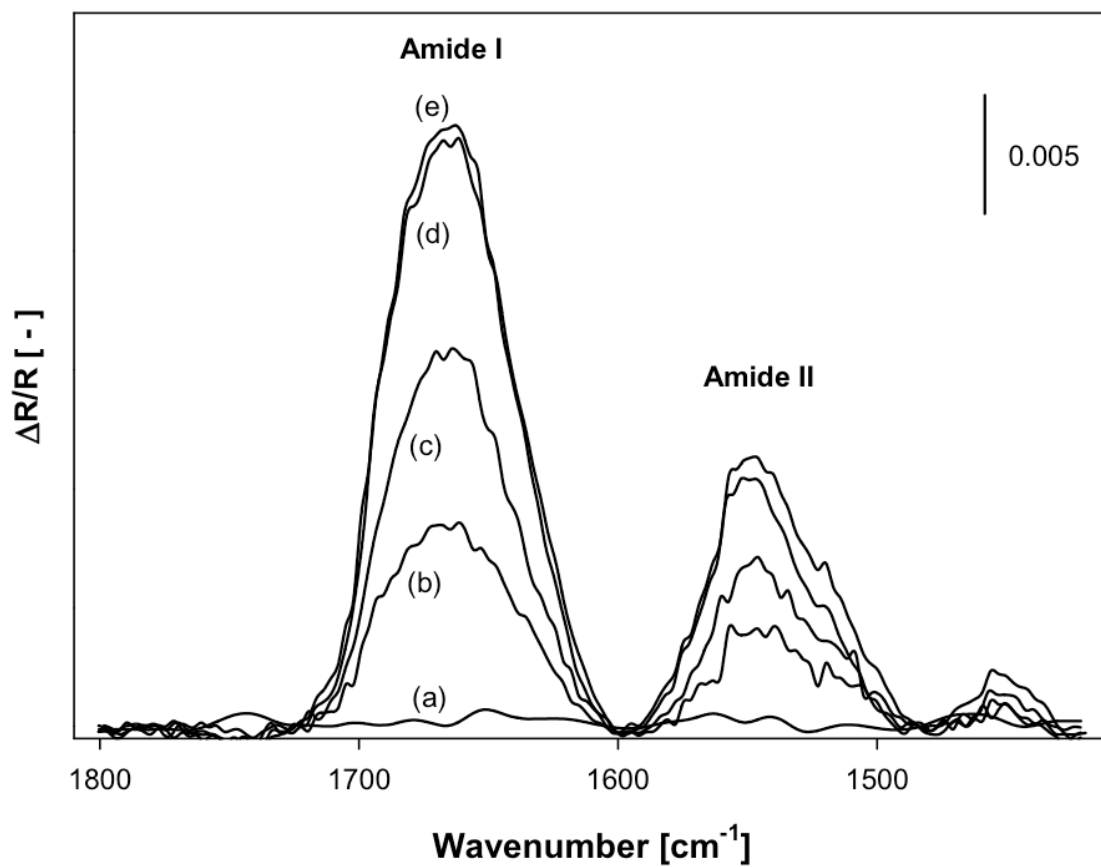


Figure 9: Typical PM-IRRAS spectra of the SS316L following immersion in phosphate buffer solution (pH 7.4) containing 0.1 g L⁻¹ of Fg after (a) 0, (b) 2, (c) 15, (d) 40 min and (e) prolonged immersion of 16 hours. Temperature = 22 °C.

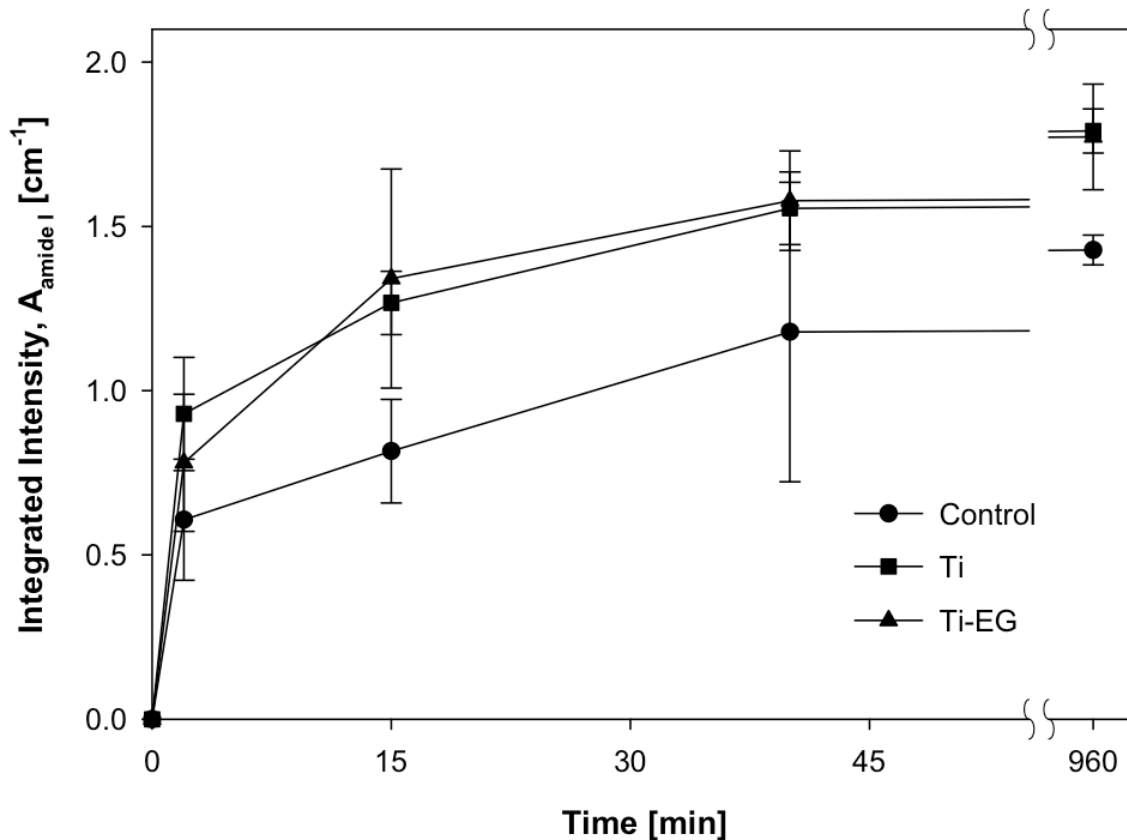


Figure 10: Variation of the Amide I integrated intensity ($A_{\text{amide I}}$) of Fg with immersion time. The data represent the area of the Amide I band of the PM-IRRAS spectra of the control, Ti and Ti+EG surfaces following immersion in phosphate buffer solution (pH 7.4) containing 0.1 g L^{-1} of Fg. The integrated intensity values refer to the projected surface area of the samples. Temperature = $22 \text{ }^{\circ}\text{C}$.

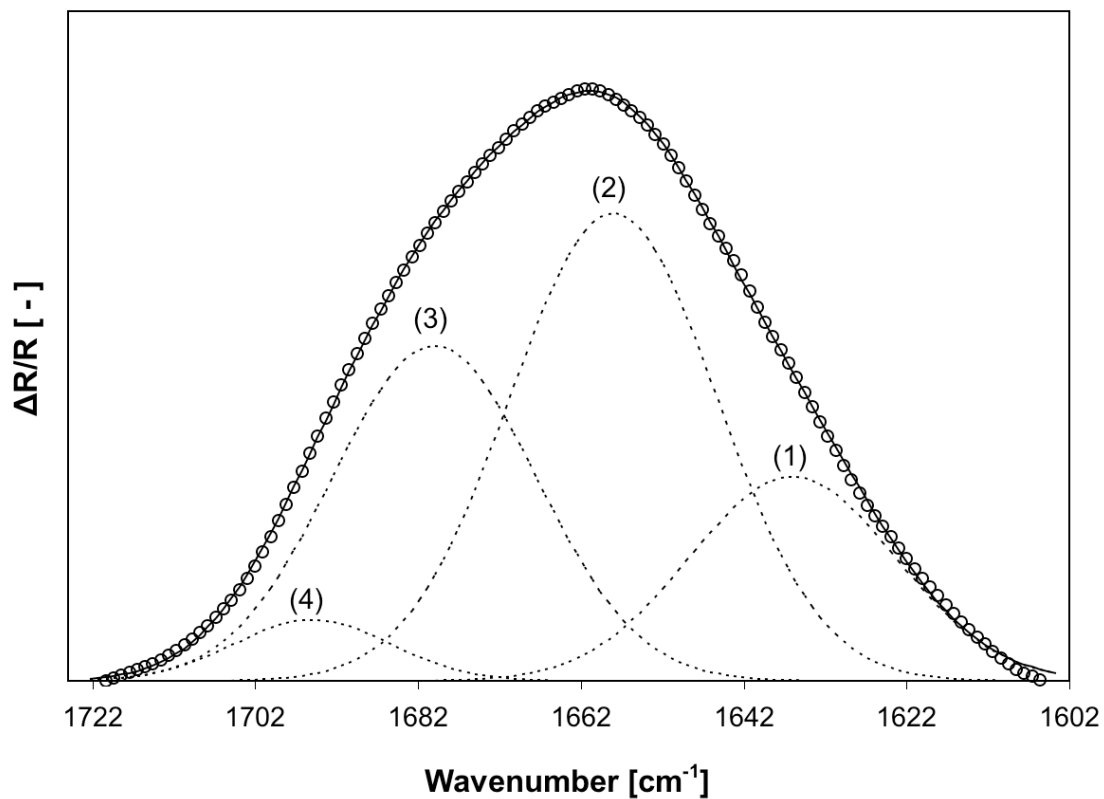


Figure 11: Amide I band and the underlying resolved components. The experimental PM-IRRAS spectrum (circle symbols) is that of the SS316L surface after a 40 min immersion in a phosphate buffer solution (pH 7.4) containing 0.1 g L⁻¹ of Fg. The sum of the fitted component bands (dashed lines) is presented by the overall simulated Amide I band (solid line). The resolved components are: (1) β -sheet, (2) α -helix, (3) β -turns, (4) contribution of CO_{COOH} stretching modes of -COOH groups in acidic amino acids (Asp and Glu).

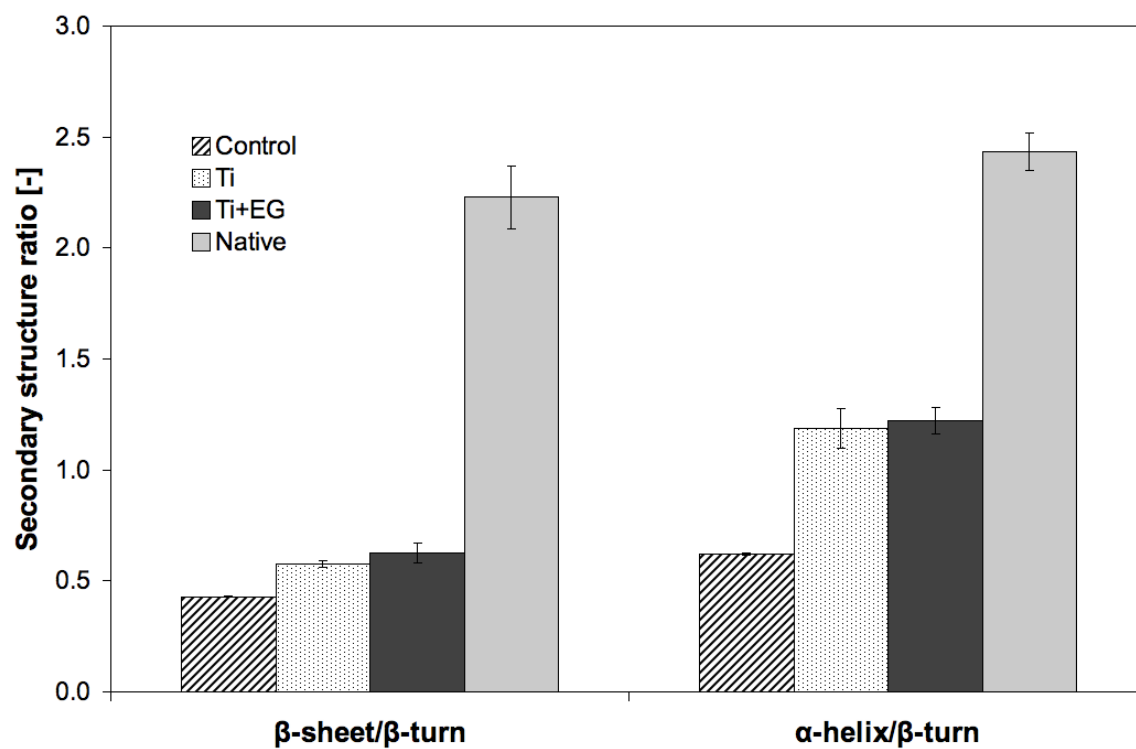


Figure 12: Ratio of the Fg secondary structure when adsorbed on the control, Ti and Ti+EG surfaces, with respect to native Fg.